Study on longitudinal modes oscillation of laser diodes based on separate and multi-mode rate differential equations

Lanping Zhang(张兰平)[1,2,3,†], Linhui Guo(郭林辉)[1,2,3], Hao Tan(谭昊)[1,2], Songxin Gao(高松信)[1,2], and Guobin Fan(范国滨)[2,4,‡]

[1] *Institute of Applied Electronics, China Academy of Engineering Physics (CAEP), Mianyang* 621900, *China*
[2] *National Key Laboratory on Advanced Laser and High Power Microwave, Mianyang* 621900, *China*
[3] *Graduate School of China Academy of Engineering Physics (CAEP), Beijing* 100088, *China*
[4] *China Academy of Engineering Physics, Mianyang* 621900, *China*

(Received 29 October 2025; revised manuscript received 23 November 2025; accepted manuscript online 25 November 2025)

Rate equations serve as a bridge between microscopic and macroscopic quantities, but it is difficult to establish a direct correlation between them. The steady-state and transient responses of multi-mode laser diodes are modeled based on multi-mode rate equations. Using the Newton iteration method, the intensities of modes of arbitrary order can be simulated, and the carrier and photon densities can be calculated. The spectrum is fitted using a symmetric distribution of different-order modes. In addition, the phenomenon of relaxation oscillation is analyzed theoretically using a numerical approach derived under the large-signal approximation. Under the small-signal approximation, the nonlinear differential equations can be simplified to linear ordinary differential equations, yielding analytical solutions from which the oscillation and damping frequencies of arbitrary orders can be determined. We demonstrate that the system is a Hamiltonian system and present its phase diagram. We reveal a time-independent relationship between the carrier and photon densities. We find that the microscopic δ factor can be characterized by the spectral width of laser diodes (LDs). The model and calculations are verified experimentally, indicating that the δ factor is estimated to be approximately 3×10^2 under free-running conditions and approximately 5×10^4 when the spectrum is locked.

Keywords: multi-mode rate equations, time dependent, spectral width, microscope characterization

PACS: 42.55.Wd, 01.55. +b, 02.60.Lj

DOI: 10.1088/1674-1056/ae23b0 **CSTR:** 32038.14.CPB.ae23b0

1. Introduction

Laser diodes (LDs) are of great importance in applications such as pump sources, laser communications, welding, and remote sensing.[1,2] A variety of LDs have been developed and have attracted increasing research interest. The laser rate equations describe the basic dynamical behavior of these systems. However, many studies have focused on single-mode operation or steady-state behavior. Few studies have investigated the dynamics of multi-mode operation and transient states, which are important for the development of multi-mode LDs and high-speed modulation chips.

Kajiyama *et al.*[3,4] investigated mode independence, competition, and dominance through rate-equation simulations. The mode interaction coefficient was varied from 0 to 5×10^3, and they revealed that an optimum relaxation coefficient exists to minimize relaxation oscillations during the rise and decay transients. The optimum value is related to the relaxation period. In addition, the dynamic characteristics of laser diodes have been calculated using single-mode rate equations that account for spontaneous emission factors. Both optical bistability (OB) and optical multistability (OM) thresholds can be controlled by the transition parameter and the Rabi probe frequency.[5] Many studies have focused on single-mode rate equations and revealed the effects of spatial hole burning, carrier-inversion moments,[6] chaos, and lasing thresholds.[13] Extrinsic and intrinsic parameters have been extracted under the small-signal approximation.[9] Jiang *et al.*[7] used a Rb-based FADOF as the frequency-selective element to achieve a continuous laser output of 103 W with a uniform circular beam. Evered *et al.*[8] used an experimental setup to investigate the relationship between optical linewidth and the reduction in speckle contrast (SC) induced by external optical feedback in a visible laser diode. By incorporating the intracavity spatial Gaussian distribution of the laser field into the rate equations, Li *et al.*[10] developed a laser-diode end-pumped, passively Q-switched, intracavity-frequency-doubling Nd:YVO4/KTP laser. The light output and electron density within the active layer of a semiconductor laser have been calculated from the steady-state solution of the rate equations. Simple analytical approximation formulas have been derived under the assumption of a power-law dependence of optical gain on electron density.[11] A large-signal model for threshold determination and operating-point selection has been discussed, and small-signal prop-

†Corresponding author. E-mail: zhanglanping_1994@163.com
‡Corresponding author. E-mail: fanguobin@caep.cn

© 2026 Chinese Physical Society and IOP Publishing Ltd. All rights, including for text and data mining, AI training, and similar technologies, are reserved.

CPB Online In Press

erties have been investigated using a state-space description of a linearized version of the rate equations based on their Jacobian.[12] The potential applications of laser-diode chaos have also been discussed, along with the availability and ease of operation of laser diodes in a wide range of configurations for exploring fundamental aspects of nonlinear and chaotic dynamics.[14] Gauge-invariant formulations and inter-mode correlations have also been investigated.[19,20] Many efforts have been made to reduce the linewidth of LDs through optical feedback from an external cavity.[15–18,21,22] Multi-mode rate equations for LDs are complex because many quantities are mutually coupled. Furthermore, laser diodes can support numerous modes due to current and temperature instabilities.

In this letter, we investigate multi-mode oscillations based on space-averaged rate equations whose independent variable is time, and analyze modes of arbitrary order using the Newton iteration method. Analytical solutions are obtained under the small-signal approximation by neglecting higher-order nonlinear terms, while numerical solutions are used to simulate the dynamics under large-signal conditions. The maximum simulated mode order is 120. An invariant quantity is identified within the adopted approximation, even under large-signal conditions. Moreover, by measuring the spectral width of a laser diode incorporating a chip-on-submount (COS) device operating in the 450 nm wavelength band, we estimate the microscopic physical quantity known as the mode interaction factor. To the best of our knowledge, the Newton iteration method has not previously been used in multi-mode rate-equation modeling. Furthermore, the simulated mode order of up to 120 is, to the best of our knowledge, the highest reported in the literature and achieved in our study.

2. Theory and simulation

We establish the theoretical model using multi-mode differential rate equations. The equations are given by[3,4]

$$\begin{cases} \dfrac{\mathrm{d}n_i}{\mathrm{d}t} = \dfrac{j}{ed} - \dfrac{n_i}{\tau_\mathrm{e}} - b_i n_i s_i - \sum\limits_{i'} \dfrac{(n_i - n_{i'})\delta_{ii'}}{M\tau_\mathrm{e}}, \\ \dfrac{\mathrm{d}s_i}{\mathrm{d}t} = b_i n_i s_i - \dfrac{s_i}{\tau_\mathrm{p}} + \beta\dfrac{n_i}{\tau_\mathrm{e}}, \end{cases} \tag{1}$$

where j denotes the current density distributed equally among the mode groups, e is the electron charge, and d is the active-layer thickness. The subscript i represents the ith-order mode, and n_i and s_i are the carrier and photon densities of the ith-order mode, respectively. M is the total number of modes, and b_i denotes the stimulated emission coefficient, given by $b_i = b_0\left[1-\gamma\frac{(i-1)^2}{M^2}\right]$, where $b_0 = 1\times10^{-6}$ cm^3/s. Here, t denotes time, τ_e and τ_p are the electron and photon lifetimes, respectively, γ is the mode-independence coefficient, β is the spontaneous emission factor, and δ is the normalized relaxation coefficient, which can also be regarded as the mode interaction factor. The selected parameters are presented in Table 1.

We now normalize the equations by introducing n_th, defined as $n_\mathrm{th} = 1/(b_0\times\tau_\mathrm{p})$, which denotes the threshold carrier density. After normalization, we define $\bar{n}_i = \frac{n_i}{n_\mathrm{th}}$, $\bar{t} = \frac{t}{\tau_\mathrm{e}}$, and $J = \frac{j\tau_\mathrm{e}}{edn_\mathrm{th}}$. These are dimensionless quantities. This normalization is intended to reduce numerical scaling issues caused by the simultaneous presence of very large and very small numbers. The differential equations can then be expressed as

$$\begin{cases} \dfrac{\mathrm{d}\bar{n}_i}{\mathrm{d}\bar{t}} = J - \bar{n}_i(1+\delta_{ii'}) - \dfrac{b_i}{b_0}\dfrac{\tau_\mathrm{e}}{\tau_\mathrm{p}}\bar{s}_i\bar{n}_i + \dfrac{\bar{n}_1+\bar{n}_2+\cdots+\bar{n}_M}{M}\delta_{ii'}, \\ \dfrac{\mathrm{d}\bar{s}_i}{\mathrm{d}\bar{t}} = \dfrac{b_i}{b_0}\dfrac{\tau_\mathrm{e}}{\tau_\mathrm{p}}\bar{s}_i\bar{n}_i - \dfrac{\tau_\mathrm{e}}{\tau_\mathrm{p}}\bar{s}_i + \beta_i\bar{n}_i. \end{cases} \tag{2}$$

The equations are nonlinear because they contain the nonlinear term $\bar{n}_i\bar{s}_i$. Therefore, they are difficult to solve directly. Analytical methods include singular perturbation expansions and perturbation methods, while numerical methods typically include the Runge–Kutta algorithm.

Table 1. Simulation parameters.

Physical quantity	Symbol	Values
Cavity layer thickness (cm)	d	5×10^{-5}
Electronic charge (C)	e	1.6×10^{-19}
Electron lifetime (ns)	τ_e	4
Photon lifetime (ps)	τ_p	1
Spontaneous emission factor	β	1×10^{-5}
Induced emission coefficient	b_i	1×10^{-6}
Normalized relaxing coefficient	δ	0–10^4
Mode dependence coefficient	γ	1.8×10^{-1}

2.1. Solution of steady state

To obtain the steady-state solutions, we set the time derivatives to zero, i.e.

$$\frac{\mathrm{d}\bar{n}_i}{\mathrm{d}\bar{t}} = 0, \quad \frac{\mathrm{d}\bar{s}_i}{\mathrm{d}\bar{t}} = 0. \tag{3}$$

Then, $\bar{n}_i$ and $\bar{s}_i$ remain constant over time. From Eq. (2), the quantitative relationship can be written as

$$\bar{s}_i = \frac{\tau_\mathrm{p}}{\tau_\mathrm{e}}\frac{\beta_i\bar{n}_i}{\left(1-\frac{b_i}{b_0}\bar{n}_i\right)}. \tag{4}$$

Substituting this expression into Eq. (2) yields the following transcendental equation:

$$J-(1+\delta_{ii'})\bar{n}_i - \frac{b_i\beta_i\bar{n}_i^2}{b_0-b_i\bar{n}_i} + \frac{\bar{n}_1+\bar{n}_2+\cdots+\bar{n}_M}{M} = 0. \tag{5}$$

Because of the denominators in this equation, direct numerical solution may fail to converge. Therefore, we rewrite the equation as follows:

$$\begin{aligned} &J(b_0-b_i\bar{n}_i) - (1+\delta_{ii'})\bar{n}_i(b_0-b_i\bar{n}_i) - b_i\beta_i\bar{n}_i^2 \\ &+\frac{\bar{n}_1+\bar{n}_2+\cdots+\bar{n}_M}{M}\delta_{ii'}(b_0-b_i\bar{n}_i) = 0. \end{aligned} \tag{6}$$

Next, we employ the Newton iteration method to solve the equation. We define the M equations as M functions

$$F(\bar{n}_i) = J(b_0-b_i\bar{n}_i) - (1+\delta_{ii'})\bar{n}_i(b_0-b_i\bar{n}_i) - b_i\beta_i\bar{n}_i^2$$

CPB Online In-Press

$$+\frac{\bar{n}_1+\bar{n}_2+\cdots+\bar{n}_M}{M}\delta_{ii'}(b_0-b_i\bar{n}_i). \tag{7}$$

We can regard these functions as an $M\times 1$ vector and calculate the corresponding $M\times M$ Jacobian matrix, denoted by $JF(\bar{n}_i)$. The initial values of $\bar{n}_i$ are set to $\bar{n}_{i0}$, and the increment is then given by

$$\bar{n}_i=\bar{n}_{i0}+\bar{x}_i,\ \ \bar{x}_i=-JF(\bar{n}_i)/F(\bar{n}_i)=-JF(\bar{n}_i)^{-1}\times F(\bar{n}_i). \tag{8}$$

The corresponding matrix representation is

$$\begin{bmatrix}x_1\\x_2\\\cdots\\x_n\end{bmatrix}=\begin{bmatrix}\frac{\partial F(\bar{n}_1)}{\partial\bar{n}_1} & \frac{\partial F(\bar{n}_2)}{\partial\bar{n}_1} & \cdots & \frac{\partial F(\bar{n}_M)}{\partial\bar{n}_1}\\ \frac{\partial F(\bar{n}_1)}{\partial\bar{n}_2} & \frac{\partial F(\bar{n}_2)}{\partial\bar{n}_2} & \cdots & \frac{\partial F(\bar{n}_M)}{\partial\bar{n}_2}\\ \cdots & \cdots & \cdots & \cdots\\ \frac{\partial F(\bar{n}_1)}{\partial\bar{n}_M} & \frac{\partial F(\bar{n}_2)}{\partial\bar{n}_M} & \cdots & \frac{\partial F(\bar{n}_M)}{\partial\bar{n}_M}\end{bmatrix}^{-1}\begin{bmatrix}F(\bar{n}_1)\\F(\bar{n}_2)\\\cdots\\F(\bar{n}_M)\end{bmatrix}. \tag{9}$$

Through successive iterations, $\bar{n}_i$ rapidly converges to its steady-state value. The corresponding values of $\bar{s}_i$ can then be determined from $\bar{n}_i$ using Eq. (4). This method allows modes of arbitrary order to be calculated. By varying δ from 0 to 1×10^4, we find that the photon density distribution becomes more uniform initially, with lower-order modes gradually dominating, indicating mode competition. In other words, the laser spectrum becomes narrower as δ increases. Thus, δ characterizes the spectral width, and its value can be estimated from the measured spectral width. However, the carrier density remains similar for different values of δ, as shown in Fig. 1. Here, J is the normalized current; $J=1$ corresponds to the threshold current.

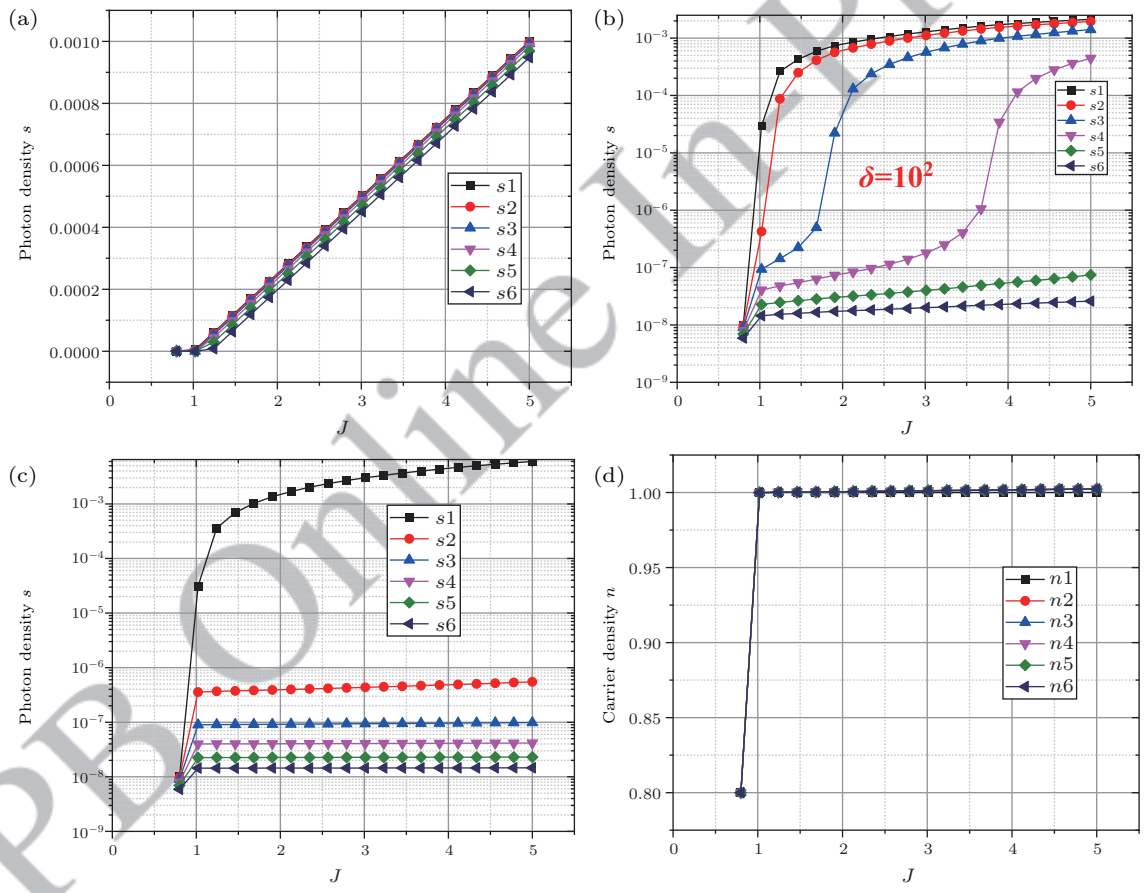


Fig. 1. Photon density versus current for (a) $\delta=0$, (b) $\delta=1\times10^2$, and (c) $\delta=1\times10^4$; (d) shows the carrier density versus current.

2.2. Solutions of transient states

2.2.1. Small-signal approximation by an analytical method

By neglecting the higher-order nonlinear terms, the nonlinear rate equations can be simplified to a set of linear ordinary differential equations. Assuming that $\bar{n}_i$ and $\bar{s}_i$ can be expressed as the sums of their steady-state values and transient perturbations, i.e., $\bar{n}_i=n_{i0}+\Delta\bar{n}_i$ and $\bar{s}_i=\bar{s}_{i0}+\Delta\bar{s}_i$, we obtain $2M$ equations comprising M equations for the carrier densities and M equations for the photon densities

$$\begin{cases}\dfrac{\mathrm{d}\Delta\bar{n}_i}{\mathrm{d}\bar{t}}=\left[-\left(1+\dfrac{M-1}{M}\delta_{ii'}\right)-\dfrac{b_i}{b_0}\dfrac{\tau_\mathrm{e}}{\tau_\mathrm{p}}\bar{s}_{i0}\right]\Delta\bar{n}_i+\dfrac{\Delta\bar{n}_1+\Delta\bar{n}_2+\cdots+\Delta\bar{n}_{i-1}+\Delta\bar{n}_{i+1}+\cdots+\Delta\bar{n}_M}{M}\delta_{ii'}-\dfrac{b_i}{b_0}\dfrac{\tau_\mathrm{e}}{\tau_\mathrm{p}}\bar{n}_{i0}\Delta\bar{s}_i,\\ \dfrac{\mathrm{d}\Delta\bar{s}_i}{\mathrm{d}\bar{t}}=\left(\dfrac{b_i}{b_0}\dfrac{\tau_\mathrm{e}}{\tau_\mathrm{p}}\bar{s}_{i0}+\beta_i\right)\Delta\bar{n}_i+\left(\dfrac{b_i}{b_0}\dfrac{\tau_\mathrm{e}}{\tau_\mathrm{p}}\bar{n}_{i0}-\dfrac{\tau_\mathrm{e}}{\tau_\mathrm{p}}\right)\Delta\bar{s}_i,\end{cases} \tag{10}$$

CPB Online In Press

where $i = 1,2,\ldots,M$. The analytical solutions can be obtained by calculating the eigenvalues and eigenvectors of the coefficient matrix above. The coefficient matrix is given by

$$Q = \left[\begin{array}{ccccc|ccccc}
-\left(1+\frac{M-1}{M}\delta_{11'}\right)-\frac{b_1}{b_0}\frac{\tau_e}{\tau_p}\bar{s}_{10} & \frac{\delta_{12'}}{M} & \frac{\delta_{13'}}{M} & \cdots & \frac{\delta_{1M'}}{M} & -\frac{b_1}{b_0}\frac{\tau_e}{\tau_p}\bar{n}_{10} & 0 & \cdots & 0 \\
\frac{\delta_{21'}}{M} & \left(1+\frac{M-1}{M}\delta_{22'}\right)-\frac{b_2}{b_0}\frac{\tau_e}{\tau_p}\bar{s}_{20} & \frac{\delta_{23'}}{M} & \cdots & \frac{\delta_{2M'}}{M} & 0 & -\frac{b_2}{b_0}\frac{\tau_e}{\tau_p}\bar{n}_{20} & \cdots & 0 \\
\cdots & \cdots & \cdots & \cdots & \cdots & \cdots & \cdots & \cdots & \cdots \\
\frac{\delta_{M1'}}{M} & \frac{\delta_{M2'}}{M} & \cdots & \frac{\delta_{M(M-1)'}}{M} & -\left(1+\frac{M-1}{M}\delta_{MM'}\right)-\frac{b_M}{b_0}\frac{\tau_e}{\tau_p}\bar{s}_{M0} & 0 & \cdots & -\frac{b_M}{b_0}\frac{\tau_e}{\tau_p}\bar{n}_{M0} & \\
\hline
\frac{b_1}{b_0}\frac{\tau_e}{\tau_p}\bar{s}_{10}+\beta_1 & 0 & 0 & \cdots & 0 & \frac{b_1}{b_0}\frac{\tau_e}{\tau_p}\bar{n}_{10}-\frac{\tau_e}{\tau_p} & 0 & \cdots & 0 \\
0 & \frac{b_2}{b_0}\frac{\tau_e}{\tau_p}\bar{s}_{20}+\beta_2 & 0 & \cdots & 0 & 0 & \frac{b_2}{b_0}\frac{\tau_e}{\tau_p}\bar{n}_{20}-\frac{\tau_e}{\tau_p} & \cdots & 0 \\
0 & 0 & \frac{b_3}{b_0}\frac{\tau_e}{\tau_p}\bar{s}_{30}+\beta_3 & \cdots & 0 & 0 & \frac{b_3}{b_0}\frac{\tau_e}{\tau_p}\bar{n}_{30}-\frac{\tau_e}{\tau_p} & \cdots & 0 \\
\cdots & \cdots & \cdots & \cdots & \cdots & \cdots & \cdots & \cdots & \cdots \\
0 & 0 & \cdots & 0 & \frac{b_M}{b_0}\frac{\tau_e}{\tau_p}\bar{s}_{M0}+\beta_M & 0 & 0 & \cdots & \frac{b_M}{b_0}\frac{\tau_e}{\tau_p}\bar{n}_{M0}-\frac{\tau_e}{\tau_p}
\end{array}\right]. \quad (11)$$

The matrix can be divided into four $M \times M$ blocks. The upper and lower blocks describe the carrier and photon densities, respectively. For $M = 6$, the system contains 12 equations. The number of distinct modes is 11 rather than 12 because the zeroth-order mode is degenerate. The photon density can be represented by s_0, $s_{\pm1}$, $s_{\pm2}$, and so on. The oscillation frequencies and damping coefficients can be determined from the eigenvalues of the coefficient matrix. The results are presented in Table 2, and the steady-state simulations are shown in Fig. 1.

Table 2. The first 6-th order analytical solutions through perturbation method.

Order	Damping frequency (Hz)	Oscillation frequency (Hz)	Modes
0-th	−35	152	n_0
1-th	−35	−152	$n_{\pm1}$
2-th	−34	133	$n_{\pm2}$
0-th	−34	−133	s_0
1-th	−74	0	$s_{\pm1}$
2-th	−184	0	$s_{\pm2}$

Furthermore, we analyze the small-signal and large-signal responses separately. The analytical solutions take an exponential form, with negative real parts and positive or negative imaginary parts in the exponents. The real parts describe decay or damping, whereas the imaginary parts describe oscillations. The general solutions can be written as

$$\begin{cases} \Delta\bar{n}_i = \sum_{m=0}^{M-1} C_{1im}\exp(-u_{1m}\bar{t}+\mathrm{j}v_{1m}\bar{t}), \\ \Delta\bar{s}_i = \sum_{m=0}^{M-1} C_{2im}\exp(-u_{2m}\bar{t}+\mathrm{j}v_{2m}\bar{t}), \end{cases} \quad (12)$$

where u_{1m} and u_{2m} denote damping coefficients, v_{1m} and v_{2m} denote oscillation frequencies, j is the imaginary unit, and C_{1im} and C_{2im} are constants. By performing matrix operations, specifically by calculating the eigenvalues and eigenvectors of Q, we can determine u, v, and C. The analytical solutions for the first six mode orders are presented in Table 2.

2.2.2. Numerical method in condition of large-scale signal

The stable solutions are obtained by solving a set of algebraic equations. First, the equations under steady-state conditions are normalized. Then, the Jacobian matrix is derived, and Newton's iteration method is used to obtain accurate solutions. Only after the stable solutions are obtained can the increments of $\bar{n}_i$ or $\bar{s}_i$ be determined.

As shown in Fig. 1, as the current J increases, the photon and carrier densities increase synchronously. The differences between modes become larger as δ increases. The spectrum can be obtained from the photon density. The photon density of each mode represents its intensity, and the mode spacing is determined by resonator parameters, including the cavity length and effective refractive index. With the intensities of different modes and the mode spacing known, the spectrum can be fitted symmetrically. Here, the modes correspond to energy levels, and the energy depends on the wavelength. Thus, the modes are longitudinal modes associated with different wavelengths.

It is difficult to solve the nonlinear differential equations directly. Therefore, the classical fourth-order, five-stage Runge–Kutta method is used to solve the nonlinear differential equations.

The relaxation time is similar under different conditions of mode interaction and is close to the carrier lifetime. The modes are symmetric: the zeroth-order mode represents the central mode, while the first-order modes correspond to ±1, and so on. Therefore, the spectrum can be fitted using the photon density distribution. From Figs. 2–4, we can observe that the differences in carrier density between different modes decrease, whereas the differences in photon density increase as δ increases. When $\delta = 0$, mode competition is weak, so the photon densities of different modes are nearly identical, whereas the carrier densities differ more noticeably, as shown in Fig. 2. When $\delta = 1 \times 10^2$, mode competition is moderate, and the lower-order modes have higher intensities. In the linear co-

CPB Online In Press

ordinate system, the photon densities of higher-order modes are very low, as shown in Fig. 3(a). Therefore, a logarithmic coordinate system is used to show the photon density distribution among different modes, as shown in Fig. 3(b). When $\delta = 1 \times 10^4$, mode competition becomes stronger, and the carrier densities of different modes become nearly identical, as shown in Fig. 4. After approximately one or two cycles, the densities tend toward steady-state values. These results indicate that mode interaction plays a dominant role in determining the photon density distribution.

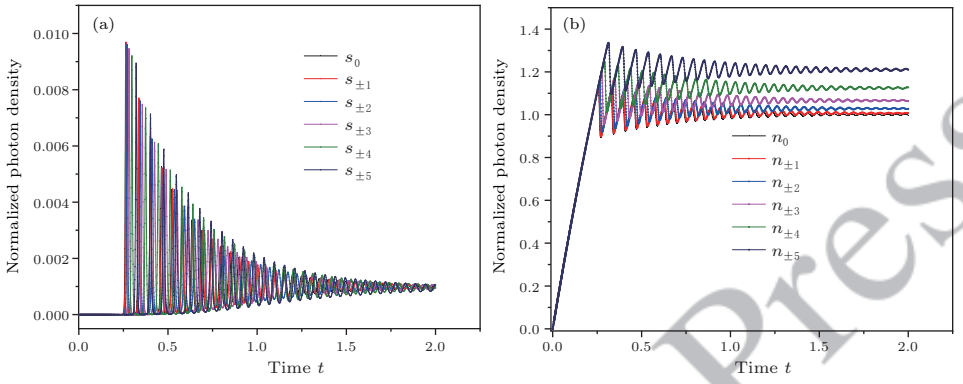


Fig. 2. The time-dependent distributions of (a) carrier density and (b) photon density when $\delta = 0$. The carrier and photon densities of different modes are similar.

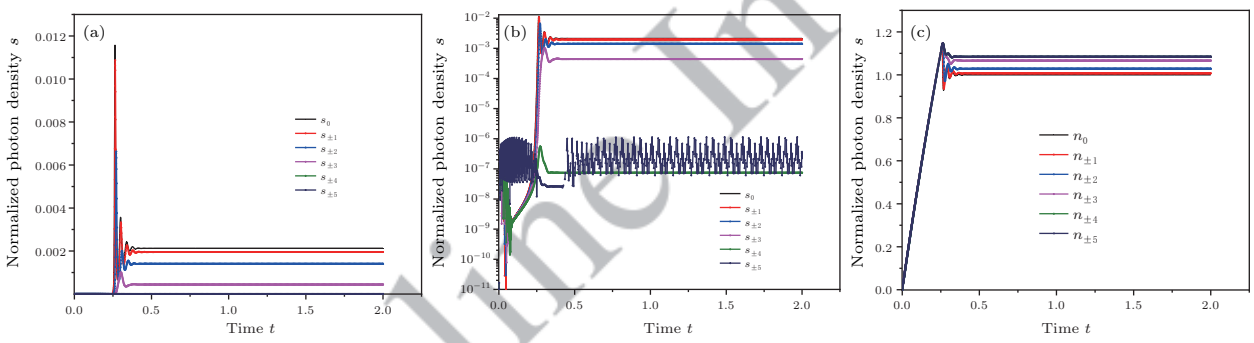


Fig. 3. (a) Photon density on a linear scale and (b) on a logarithmic scale as functions of time when $\delta = 1 \times 10^2$; (c) shows the carrier density. The photon and carrier densities of different modes differ, indicating moderate mode competition.

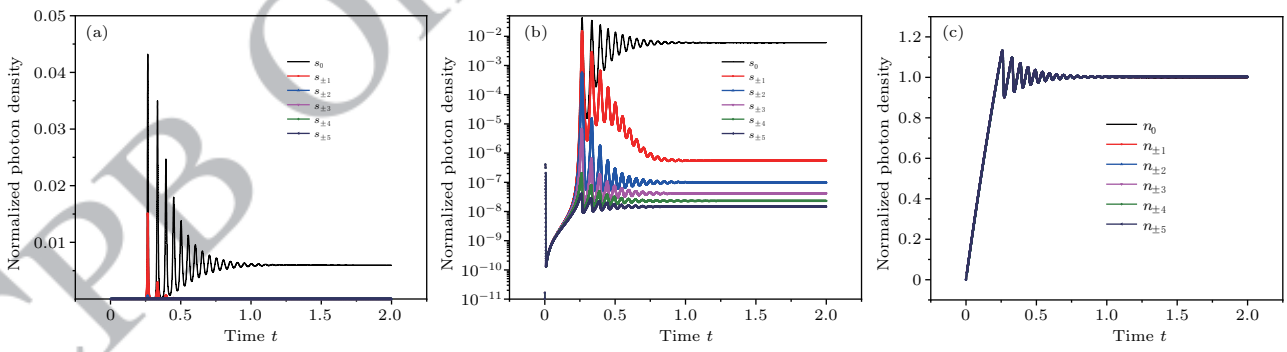


Fig. 4. (a) Carrier density on a linear scale and (b) on a logarithmic scale as functions of time when $\delta = 1 \times 10^4$; (c) shows the photon density. The photon densities of different modes differ, whereas the carrier densities are nearly identical, indicating strong mode competition.

2.3. Phase portrait and Hamilton invariant

We consider the phase portrait of the dependent variables to quantitatively describe their relationship. Taking the first-order mode as an example, the original equations are

$$\begin{cases} \dfrac{\mathrm{d}\Delta\bar{n}_1}{\mathrm{d}t} = \left(-1 - \dfrac{b_1}{b_0}\dfrac{\tau_\mathrm{e}}{\tau_\mathrm{p}}\bar{s}_{10}\right)\Delta\bar{n}_1 - \dfrac{b_1}{b_0}\dfrac{\tau_\mathrm{e}}{\tau_\mathrm{p}}\bar{n}_{10}\Delta\bar{s}_1, \\ \dfrac{\mathrm{d}\Delta\bar{s}_1}{\mathrm{d}t} = \left(\dfrac{b_1}{b_0}\dfrac{\tau_\mathrm{e}}{\tau_\mathrm{p}}\bar{s}_{10} + \beta\right)\Delta\bar{n}_1 + \left(\dfrac{b_1}{b_0}\dfrac{\tau_\mathrm{e}}{\tau_\mathrm{p}}\bar{n}_{10} - \dfrac{\tau_\mathrm{e}}{\tau_\mathrm{p}}\right)\Delta\bar{s}_1. \end{cases} \tag{13}$$

Dividing the first equation by the second yields the relationship between the carrier and photon densities. This relationship between the dependent variables is plotted in Fig. 5.

A phase singularity represents the steady state, while the orbit curves characterize the system dynamics. As δ increases, the phase orbits surround a set of similar points and tend to converge.

The governing equations can be transformed into an algebraic equation by dividing the first equation by the second equation in Eq. (13). This yields a first-order ordinary differ-

CPB Online In-Press

ential equation. By applying the method of first integration, an invariant quantity can be obtained. Through this derivation, the Hamiltonian is given by

$$H = \frac{\left(C\frac{\Delta\bar{s}_1}{\Delta\bar{n}_1} + G\right)^{\frac{P}{C}}}{\left(-\frac{\Delta\bar{s}_1}{\Delta\bar{n}_1} + Q\right)^{K}} \Delta\bar{n}_1. \tag{14}$$

Here, G, P, Q, and K are constants. The results indicate that the system conserves a quantity analogous to energy. Equation (13) can be rewritten as

$$\begin{cases} \dfrac{\mathrm{d}\Delta\bar{n}_1}{\mathrm{d}t} = B\Delta\bar{n}_1 + C\Delta\bar{s}_1, \\ \dfrac{\mathrm{d}\Delta\bar{s}_1}{\mathrm{d}t} = E\Delta\bar{n}_1 + F\Delta\bar{s}_1. \end{cases} \tag{15}$$

The constants G, P, Q, and K are determined by

$$Q = \frac{(F-B) \pm \sqrt{(B-F)^2 + 4CE}}{2C}, \quad G = E/Q,$$
$$P = \frac{(B-Q)C}{Q(C+1)}, \quad K = 1 + P/C. \tag{16}$$

The Hamiltonian system is derived from the original rate equations under the small-signal approximation. The carrier density n and photon density s form a system governed by the differential equations in Eq. (15). After first integration, a constant of motion that does not vary with n or s is obtained; this constant is the Hamiltonian. The phase portrait illustrates the relationship between the carrier and photon densities, while the orbit curves qualitatively reveal the system's conservation properties. The analysis focuses on limit cycles, phase singularities, and periodic motion.

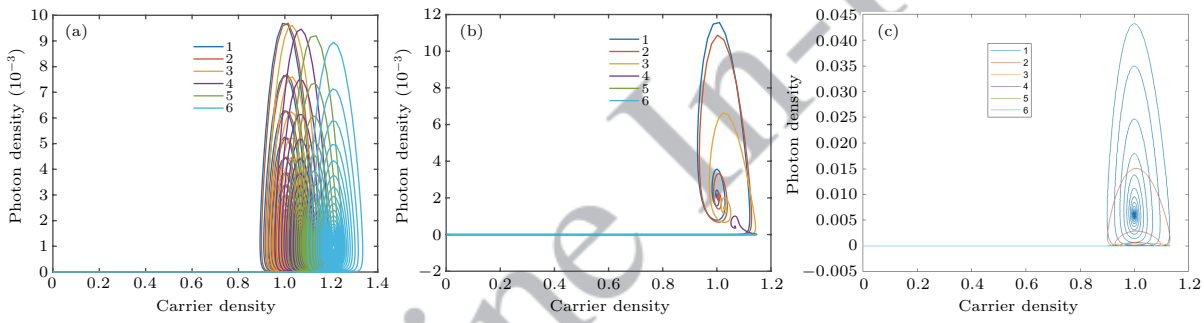


Fig. 5. Phase portraits for increasing mode interaction coefficient δ: (a) $\delta = 0$, (b) $\delta = 1 \times 10^2$, and (c) $\delta = 1 \times 10^4$.

3. Experimental results and discussion

A 450 nm wavelength COS (chip on submount) chip is used in the experiment. The stripe width is 45 μm, the waveguide thickness is approximately 1 μm, and the divergence angles along the fast and slow axes are 50° and 10°, respectively. The physical dimensions of the COS package and the die chip are 4 mm × 3 mm × 0.42 mm and 1.2 mm × 0.15 mm × 0.085 mm, respectively. The focal lengths of the fast-axis and slow-axis collimation lenses are 0.3 mm and 9 mm, respectively. The chip parameters are listed in Table 3. The free-running and wavelength-locked spectra, as well as the time-domain signals, are measured using a high-precision spectrometer with a high sampling rate and wide bandwidth. The experimental setup is shown in Fig. 7.

The theoretical photon density is shown in Fig. 6. As can be seen, the photon densities of different modes reach steady-state values after approximately 0.5 time units. The corresponding relative mode intensities, which are proportional to the photon densities, are distributed among different longitudinal modes with equal spacing. The spectrum can then be obtained, allowing the spectral width to be estimated.

The length of the COS chip is 1.2 mm, and the refractive index of the GaN-based chip is 2.2. Therefore, the longitudinal mode spacing can be determined using the following formula:

$$\Delta\nu = \frac{c}{2\eta L}, \tag{17}$$

where c is the speed of light, L is the cavity length, and η is the refractive index of the medium. Furthermore, the wavelength spacing can be determined by

$$\Delta\lambda = \frac{\lambda^2}{c}\Delta\nu = \frac{\lambda^2}{2\eta L}. \tag{18}$$

Table 3. Parameters of Chip.

Parameters of COS chip	Values
Strip width (μm)	45
Central wavelength (nm)	440–450 nm
Waveguide thickness (μm)	< 1
Divergence (degrees)	50° along fast axis, 10° along slow axis
Physical size of COS (mm) (length × width × thickness)	4 × 3 × 0.42
Physical size of chip (mm) (length × width × thickness)	1.2 × 0.15 × 0.085

By adjusting the mode interaction coefficient δ, we can obtain mode intensity distributions such as those shown in Fig. 6. The steady-state mode intensities can then be extracted as a function of wavelength. If the calculated spectrum agrees well with the measured spectrum, the selected value of δ is

CPB Online In-Press

considered appropriate. The calculated wavelength spacing is approximately 0.035 nm, allowing the number of modes to be determined. The total number of modes is set to 60. After the calculation, the estimated value of δ is approximately 3×10^2 under free-running conditions and approximately 5×10^4 under wavelength-locked conditions, with the spontaneous emission coefficient set to 1×10^{-5} in both cases. The measured and fitted spectra are shown in Figs. 8 and 9.

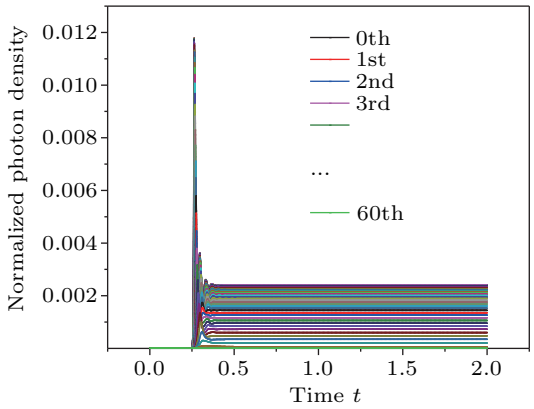


Fig. 6. Normalized photon density as a function of time, with 60 and 120 modes included in the simulation together with the carrier density.

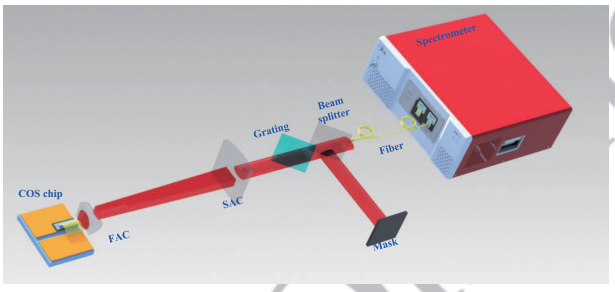


Fig. 7. Schematic of the experimental setup. FAC denotes fast-axis collimation, and SAC denotes slow-axis collimation. The beam splitter reflects and transmits 50% of the incident laser beam to the mask and spectrometer, respectively.

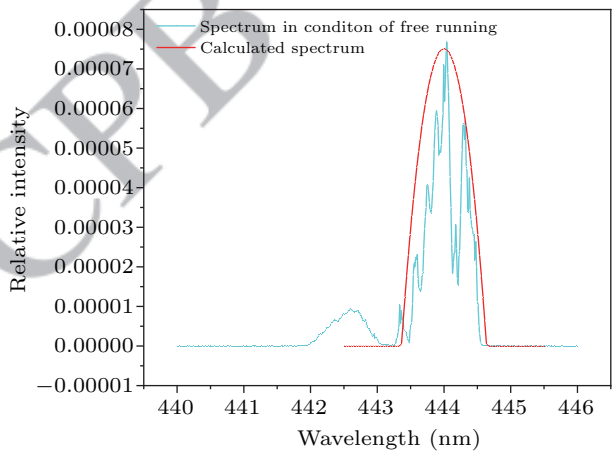


Fig. 8. Measured free-running spectrum and the corresponding fitted spectrum obtained from calculations.

We can see that the spectral width of the free-running laser, assessed by the FWHM (full width at half maximum), is about 1 nm, with approximately 32 modes. The calculated spectral width is 1.05 nm. After locking, the spectral width decreases to about 0.1 nm, with approximately 3 modes. In practice, the measured spectrum is asymmetric. We speculate that this asymmetry is caused by spatial hole burning, which leads to a nonuniform gain spectrum. Therefore, the agreement between the measured and fitted spectra is limited, although their spectral widths are similar.

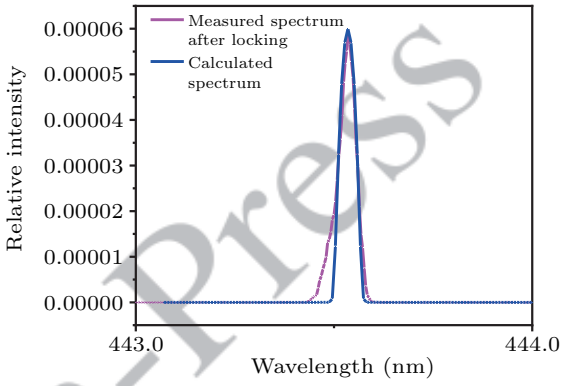


Fig. 9. Measured wavelength-locked spectrum and the corresponding fitted spectrum obtained from calculations.

4. Conclusion and perspectives

The first 60 modes (120th order when combined with the carrier density) are described using the results of the multimode rate equations. A model incorporating all relevant parameters is established, allowing the spectra in the steady state and transient state, as well as the fitted spectra, to be plotted by varying parameters such as the mode interaction factor, spontaneous emission factor, current, and time. The steady-state solutions reveal the relationship between the mode interaction coefficient and the spectral width. The transient-state solutions indicate a relationship between the relaxation oscillation time and the carrier lifetime. The experimentally measured spectral widths (FWHM) agree well with the simulations. This approach to estimating microphysical quantities can provide a foundation for developing accurate models for a wide range of applications.

Acknowledgments

We thank our project partners for their assistance and fruitful discussions. We also acknowledge the support of the Military Civilian Integration Fund of the Chinese Academy of Engineering Physics.

References

[1] Wierer J J, Tsao J Y and Sizov D S 2013 *Laser Photonics Rev.* **7** 963
[2] Jechow A 2010 *Laser Photonics Rev.* **4** 633
[3] Kajiyama K, Hata S and Sakata S 1977 *Appl. Phys.* **12** 209
[4] Kajiyama K, Hata S and Sakata S 1978 *Appl. Phys.* **16** 155
[5] Hameed A H, Hadi S, Hachim F K, Al Nashy B O and Al-Khursan A H 2025 *Chin. J. Phys.* **94** 241
[6] Lenstra D and Mirvais 2014 *Opt. Express* **22** 8143
[7] Jiang L, Wang R and Zhao H 2024 *High Power Laser Sci. Eng.* **12** e73

CPB Online In-Press

[8] Evered C, Li K and Fan Y 2024 *Opt. Lett.* **49** 3524
[9] Gao J, Li X and Flucke J 2004 *J. Lightwave Technol.* **22** 1604
[10] Li G, Zhao S and Zhao H 2004 *Opt. Commun.* **234** 321
[11] Salathé R, Voumard C and Weber H 1974 *Opto-electronics*
[12] Schaer T, Rusnov R and Eagle S 2003 *IEEE* 1226399
[13] Adams M J 1973 *Opto. Electron.* **5** 201
[14] Sciamanna M and Shore K A 2015 *Nat. Photonics* **9** 151
[15] Wenzel S 2022 *Laser Photonics Rev.* 16
[16] Kang J H, Wenzel H and Freier E 2022 *Photonics Res.* **10** 1157
[17] Wang J, Hu J and Guan C 2024 *Photonics Res.* **12** 1186
[18] Zhong Z, Chang D and Jin W 2021 *Photonics Res.* **9** 1336
[19] Marin F, Bramati A and Giacobino E 1995 *Phys. Rev. Lett.* **75** 4606
[20] Parks A M, Moloney J V and Brabec T 2023 *Phys. Rev. Lett.* **131**
[21] Zhang L, Jiang Q and Wang C 2025 *Opt. Express* **33** 18291
[22] Zhang L, Tan H and Guo L 2020 *Proc. SPIE* **11617** 904

CPB Online In-Press